Half-lives and branchings for β-delayed neutron emission for neutron-rich Co–Cu isotopes in the r-process

P. Hosmer,[1,2] H. Schatz,[1,2,3] A. Aprahamian,[4] O. Arndt,[5,6] R. R. C. Clement,[1,*] A. Estrade,[1,2] K. Farouqi,[7,†] K.-L. Kratz,[6,8] S. N. Liddick,[1,9] A. F. Lisetskiy,[10] P. F. Mantica,[1,9] P. Möller,[11] W. F. Mueller,[1] F. Montes,[1,2] A. C. Morton,[1,‡] M. Ouellette,[1,2] E. Pellegrini,[1,2] J. Pereira,[1] B. Pfeiffer,[5,6] P. Reeder,[12] P. Santi,[1,§] M. Steiner,[1] A. Stolz,[1] B. E. Tomlin,[1,9] W. B. Walters,[13] and A. Wöhr[14]

[1]*National Superconducting Cyclotron Laboratory, Michigan State University, East Lansing, Michigan 48824, USA*
[2]*Department of Physics and Astronomy, Michigan State University, East Lansing, Michigan 48824, USA*
[3]*Joint Institute for Nuclear Astrophysics, Michigan State University, East Lansing, Michigan 48824, USA*
[4]*Department of Physics and Joint Institute for Nuclear Astrophysics, University of Notre Dame, Notre Dame, Indiana 46556, USA*
[5]*Institut für Kernchemie, Universität Mainz, Fritz-Strassmann Weg 2, D-55128 Mainz, Germany*
[6]*HGF Virtuelles Institut für Kernstruktur und Nukleare Astrophysik*
[7]*Department of Astronomy and Astrophysics and Joint Institute for Nuclear Astrophysics, University of Chicago, Chicago, IL 60637, USA*
[8]*Max-Planck-Institut für Chemie (Otto-Hahn-Institut), J.-J.-Becherweg 27, D-55128 Mainz, Germany*
[9]*Department of Chemistry, Michigan State University, East Lansing, Michigan 48824, USA*
[10]*Department of Physics, University of Arizona, Tucson, Arizona 85721, USA*
[11]*Theoretical Division, Los Alamos National Laboratory, Los Alamos, New Mexico 87545, USA*
[12]*Pacific Northwest National Laboratory, MS P8-50, P.O. Box 999, Richland, Washington 99352, USA*
[13]*Department of Chemistry and Biochemistry, University of Maryland, College Park, Maryland 20742, USA*
[14]*Department of Physics, University of Notre Dame, Notre Dame, Indiana 46556-5670, USA*

(Received 8 March 2010; published 18 August 2010)

The β decays of very neutron-rich nuclides in the Co–Zn region were studied experimentally at the National Superconducting Cyclotron Laboratory using the NSCL β-counting station in conjunction with the neutron detector NERO. We measured the branchings for β-delayed neutron emission (P_n values) for ^{74}Co ($18 \pm 15\%$) and $^{75-77}$Ni ($10 \pm 2.8\%$, $14 \pm 3.6\%$, and $30 \pm 24\%$, respectively) for the first time, and remeasured the P_n values of $^{77-79}$Cu, ^{79,81}Zn, and ^{82}Ga. For $^{77-79}$Cu and for ^{81}Zn we obtain significantly larger P_n values compared to previous work. While the new half-lives for the Ni isotopes from this experiment had been reported before, we present here in addition the first half-life measurements of ^{75}Co (30 ± 11 ms) and ^{80}Cu (170^{+110}_{-50} ms). Our results are compared with theoretical predictions, and their impact on various types of models for the astrophysical rapid neutron-capture process (r-process) is explored. We find that with our new data, the classical r-process model is better able to reproduce the $A = 78$–80 abundance pattern inferred from the solar abundances. The new data also influence r-process models based on the neutrino-driven high-entropy winds in core collapse supernovae.

DOI: 10.1103/PhysRevC.82.025806 PACS number(s): 26.30.Hj, 21.10.Tg, 23.40.−s, 27.50.+e

I. INTRODUCTION

The rapid neutron-capture process (r-process) is traditionally believed to produce roughly half of the heavy elements beyond the iron region [1–3]. The site of the r-process is still not known with certainty. The necessary very high densities of free neutrons require extreme conditions that have been proposed to be encountered in various sites within core collapse supernovae, for example, the neutrino-driven wind in delayed explosion models [4–6], jets [7], fallback material [8], or, maybe, prompt explosions [9,10]. Alternatively, the r-process could also occur in neutron star mergers [11], γ-ray bursts [12,13], or quark novae [14]. What is known from observations is the pattern of isotopic and elemental abundances that the r-process produces. This r-process abundance pattern can be extracted from the Solar System abundances by subtracting the contributions from the s- and p-processes. It can also be observed directly in a specific class of extremely metal poor but r-process element enhanced stars in the halo of the Galaxy (for a recent review, see [15]). More than two dozen of such stars have been found so far revealing a consistent r-process pattern for elements from Ba to the Pt peak, but showing variations for lighter and heavier elements. Ongoing large-scale surveys of Galactic halo stars together with high-resolution spectroscopic followups are expected to find many more such stars in the future. This continuously increasing body of observational information needs to be compared and interpreted with r-process models for the various sites that have been proposed. This requires a solid understanding of the underlying nuclear physics, which can have as much influence on the r-process abundances as the astrophysical environment [16–18]. Currently, nuclear physics

*Current address: Applied Physics Division, Los Alamos National Laboratory, Los Alamos, NM 87545, USA.
†Current address: Landessternwarte, Universität Heidelberg, Känigstuhl 12, D-69117 Heidelberg, Germany.
‡Current address: TRIUMF, 4004 Wesbrook Mall, Vancouver, British Columbia V6T 2A3, Canada.
§Current address: Los Alamos National Laboratory, Los Alamos, NM, USA.

uncertainties prevent the reliable extraction of site-specific signatures from observational data and reliable calculation of the nucleosynthesis products of a specific r-process scenario.

Most models assume that the r-process is a sequence of rapid neutron captures and β decays. Neutrino interactions and fission processes might play some role depending on the specific r-process environment. Among the most important nuclear physics quantities needed in r-process models are the β-decay half-lives of the r-process waiting points, which determine directly the process time scale and the produced abundance level at their location in the path. Branchings for β-delayed neutron emission are also important [16] during and after the r-process freezes out and the unstable nuclei along the r-process path decay toward stability. β-delayed neutron emissions during that stage modify the final abundances and increase the neutron abundance during freeze-out. In recent years great progress has been made in experimentally determining β-decay properties of nuclei relevant to the r-process [19–28]. Nevertheless, only a very small fraction of the r-process isotopes have been reached experimentally so far, most of them located near or in between the $N = 50$ and $N = 82$ shell closures. r-process model calculations therefore rely on global theoretical models for the prediction of β-decay properties far from stability. These models have to be tested systematically by comparison with experimental data along isotopic chains far from stability.

This collaboration has reported half-life measurements of the waiting point nucleus ^{78}Ni and other neutron-rich Ni isotopes performed at the National Superconducting Cyclotron Laboratory (NSCL) at Michigan State University [25]. With this measurement, the half-lives of all the relevant $N = 50$ waiting points in the r-process, ^{78}Ni, ^{79}Cu, and ^{80}Zn, are known experimentally. This mass region plays a critical role in the subset of r-process models (for example, Refs. [10,16,29]) that are characterized by a neutron-capture flow through $N = 50$, where it represents the first major bottle-neck for the production of heavier nuclei after the $A = 8$ stability gap.

In this paper we present β-decay half-lives and branchings for β-delayed neutron emission for a range of very neutron-rich Co, Ni, Cu, and Zn isotopes obtained in the same experiment. These data provide tests for theoretical models used to predict β-decay properties for r-process model calculations. In particular, the combined measurement of the half-life and the branching for β-delayed neutron emission provides a stringent test probing the β-strength function at low excitation energies and just above the neutron threshold [30]. In addition, improved data on the branchings for β-delayed neutron emission of ^{78}Cu and ^{79}Cu are direct input in r-process model calculations. They determine the final abundance pattern produced by the decay of the abundances accumulated during the r-process at the $N = 50$ waiting point nuclei.

The region around ^{78}Ni is also of considerable interest for nuclear physics. In general, doubly magic nuclei provide a testing ground for single-particle structure and shell models, which in the cases of ^{78}Ni and ^{132}Sn are uniquely located at extreme neutron excess. Consequently, a great deal of experimental [31–38] and theoretical [38–47] activity has been devoted to nuclei near ^{78}Ni. An example is the existence of 8^+ seniority isomers that is now established in ^{70}Ni [31], ^{76}Ni [36,37], and ^{78}Zn [40] and is interpreted as evidence of the persistence of strong shell gaps out to ^{78}Ni. The nonexistence of these isomers in ^{72}Ni and ^{74}Ni [34] is now explained with a subtle change in the residual nucleon-nucleon interaction. Another example is the shift of the $f_{5/2}$ proton orbital observed in the odd-A Cu isotopes with increased filling of the neutron $g_{9/2}$ orbital due to the monopole term in the proton-neutron residual interaction [33,44]. An understanding of these nuclear structure effects around ^{78}Ni requires reliable shell model calculations [38,40,41,44]. Recently some efforts have been made to develop a new effective shell model interaction for this region (JJ4A) [46]. Our new data provide a test for how well these shell model calculations extrapolate to the most neutron-rich nuclei.

II. SETUP

Extremely neutron-rich nuclei were produced at the NSCL by fragmentation of a 15 pnA 140 MeV/nucleon ^{86}Kr^{34+} primary beam on a 376 mg/cm^2 Be target. After separation with the A1900 fragment separator using the $B\rho$-ΔE-$B\rho$ method [48], the mixed beam was implanted continuously into the NSCL β-counting system (BCS) [49] consisting of a stack of Si PIN detectors, a double-sided Si strip detector (DSSD) for implantation of the ions, and a set of six single-sided Si strip detectors (SSSDs) followed by two additional Si PIN diodes (see Fig. 1).

Each implanted ion was identified event-by-event through a measurement of its magnetic rigidity, which in connection with a time-of-flight measurement provides the mass to charge ratio, and energy loss in the Si PIN detectors, which provides information about the atomic number. The magnetic rigidity was determined by a position measurement at the intermediate dispersive image of the A1900 fragment separator using a position sensitive plastic scintillator. Time-of-flight was measured between two plastic scintillators located at the exit of the A1900 and in front of the BCS. The resulting particle identification spectrum can be found in Ref. [25]. The implantation detector was a 985 μm thick DSSD with 40 $\times$ 40 pixels registering time and position of ion implantations and β decays. To increase the β-decay correlation efficiency,

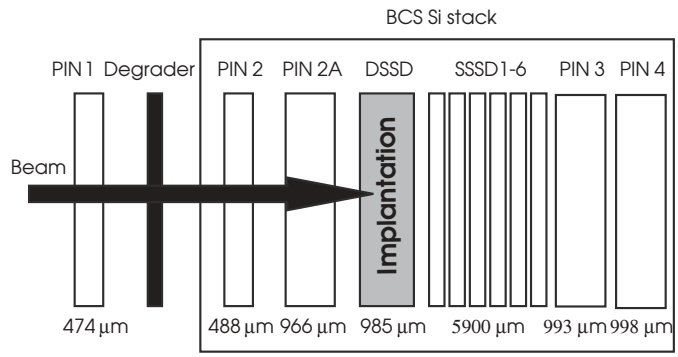

FIG. 1. Schematic arrangement of the Si detectors comprising the NSCL β-counting system in the configuration used for this experiment. The degrader was adjusted to ensure implantation within the DSSD.

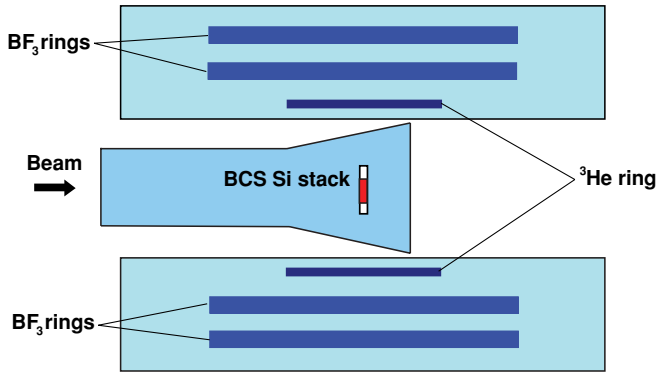

FIG. 2. (Color online) Schematic arrangement of the BCS within the NERO neutron detector.

correlations between decays and preceding implantations were established using a 3×3 pixel area centered around the implantation location. The total implantation rate into all 1600 pixels of the BCS was always less than 0.1 ions per second, providing enough time between implantations into the same 3×3 pixel area for all decays of interest to occur long before the implantation of the next ion. The SSSDs and the downstream Si PIN diodes were used to veto beam contaminants that were not stopped in the DSSD.

In this paper, we also present results from NERO (neutron emission ratio observer), a neutron detector that surrounded the BCS to provide information about branchings for β-delayed neutron emission [50] (see Fig. 2 and Refs. [26,28]).

NERO is a neutron long counter consisting of 60 ionization counters filled with BF_3 or ^{3}He gas imbedded in a block of polyethylene. The counters are arranged in three concentric rings around the beam axis with the inner ring using ^{3}He detectors, while the two outer rings use BF_3 gas counters. The center of the detector is a cylindrical cavity with 22.4 cm diameter containing the beam line and the BCS, with the center of the DSSD being located in the center of the NERO detector. Neutrons emitted in the DSSD during β decay of a neutron-rich isotope are thermalized in the polyethylene and then detected either by a ^{10}B(n,α) reaction in a BF_3 gas counter or a ^{3}He(n,p) reaction in a ^{3}He gas counter. Neutron detection events are registered using a multi-hit time-to-digital converter (TDC) for each of the 60 detectors that is started with the detection of the β-decay event in the DSSD. The typical thermalization time scale for neutrons with initial energies of a few MeV (for example, for a ^{252}Cf source) is of the order of 70 μs. To determine whether a neutron has been emitted after a β decay, we therefore count neutrons for a 200 μs time period. This is sufficient to detect most neutrons (about 96%) [50]. With our low overall implantation rate of less than 0.1 ions per second, this is still fast enough to correlate the neutron detection uniquely with a β-decay event and the preceding implantation event.

III. RESULTS FOR β-DECAY HALF-LIVES

The mixed rare isotope beam used in this experiment contained $^{73-75}$Co, $^{75-78}$Ni, $^{77-80}$Cu, and $^{79-81}$Zn as well as smaller amounts of the more stable isotopes $^{81-82}$Ga, ^{76}Cu, and ^{74}Ni. β-decay half-lives were determined as described in Ref. [25] using a maximum likelihood analysis method (MLH) [28]. The likelihood function to be maximized is the product of the probability densities for each implantation event describing the measured time sequence of decay-type events following the implantation within a correlation time $\tau_{\rm corr}$. The formalism takes into account three decay generations and a constant background. For this analysis we used $\tau_{\rm corr} = 5$ s. We also take into account β-delayed neutron emission for the parent and daughter nuclei, which changes the daughter and grand-daughter half-lives. The only free parameter is the assumed parent half-life. Daughter half-lives and P_n values are fixed and were taken from the literature [51] and [21] or, when available, from this experiment. The advantage of this method is that it avoids the loss of information about the exact time, pixel location, and time sequence of the multiple decay events following individual implantations of parent nuclei that occurs when binning events to form decay curves.

To determine the detection efficiency for β particles, we performed a traditional decay curve analysis for the cases with high statistics that included ^{75}Ni, ^{76}Ni, ^{77}Cu, ^{78}Cu, ^{79}Zn, and ^{80}Zn. The half-lives obtained from the fits agree with the ones from the MLH analysis. The β-decay detection efficiencies for the DSSD can be determined from the parent decay component and the known number of implantation events. The resulting efficiencies varied for different isotopes from 40.7% to 43.0%, in some cases by more than the statistical one-sigma errors, but without any obvious trend. For the isotopes with less statistics, we therefore assumed an average β detection efficiency of $42 \pm 1\%$ for all three generations.

The background rate for decay-type events was determined for each implantation pixel and for each run (typically an hour long) by counting all decay events outside of a 100 s time window following an implantation that occurred in the corresponding correlation area. Typical background rates during the experiment ranged from 0.008 to 0.015 s^{-1} averaged over the entire detector. The largest background rate was found near the center of the DSSD, where implantation rates are highest, with a smooth decrease by about a factor of 10 toward the detector edges. This position- and run-dependent background rate was compared with the background rate determined from decay curve fits by averaging over the particular implantation pattern (pixel and run) for the individual isotope and agreed reasonably well.

The resulting β-decay half-lives together with the number of implanted isotopes are listed in Table I. For the convenience of the reader, we include our previously published half-lives for the Ni isotopes [25].

The errors include statistical and systematic errors. The statistical error is obtained from the maximum likelihood analysis. To determine the systematic error, we recalculated half-lives for all possible variations in the input parameters such as efficiency, P_n values, and half-lives of later decay generations. The envelope of all half-lives with their statistical errors was then used as an estimate for the total error. Systematic errors typically represent a small fraction of the total error. Contributions of the order of 20–30% of the total

TABLE I. Number of detected implanted ions $N_{\rm imp}$, half-lives $T_{1/2}$ from this and previous work, number of detected correlated β-n coincidences $N_{\beta n}$, number of expected background β-n coincidences from random background and daughter decays $N_{\beta nb+d}$, and P_n values from this and previous work [21,52].

Nuclide	$N_{\rm imp}$	$T_{1/2}$ (ms)		$N_{\beta n}$	$N_{\beta nb+d}$	P_n (%)	
		This work	Previous			This work	Previous
^{73}Co	420	$41.\pm 6$	41 ± 4	4	2.1	<7.9	>9
^{74}Co	331	$34.^{+6}_{-9}$	30 ± 3	16	7.9	18 ± 15	>26
^{75}Co	76	$30.\pm 11$		1	1.4	<16	
^{75}Ni	1905	$344.\pm 25$	600 ± 200	43	16	10 ± 2.8	
^{76}Ni	1441	$238.\pm 18$	470 ± 390	43	13	14 ± 3.6	
^{77}Ni	159	$128.^{+36}_{-32}$		13	6.2	30 ± 24	
^{78}Ni	13	$110.^{+100}_{-60}$		3	0.8		
^{76}Cu	277	$599.\pm 18$	641 ± 6	3	2.4	<7.2	2.4 ± 0.5
^{77}Cu	6771	$466.^{+21}_{-20}$	469 ± 8	348	35	31 ± 3.8	$15\,^{+10}_{-5}$
^{78}Cu	4653	$335.\pm 17$	342 ± 11	310	24	44 ± 5.4	$15\,^{+10}_{-5}$
^{79}Cu	754	$257.^{+29}_{-26}$	188 ± 25	81	4.2	72 ± 12	55 ± 17
^{80}Cu	16	$170.^{+110}_{-50}$		0	0.1		
^{79}Zn	2109	$746.\pm 42$	995 ± 19	19	13	2.2 ± 1.4	1.3 ± 0.4
^{80}Zn	5043	$578.\pm 21$	545 ± 16	45	40	<1.8	1 ± 0.5
^{81}Zn	229	$474.^{+93}_{-83}$	290 ± 50	14	4.2	30 ± 13	7.5 ± 3
^{81}Ga	75	$959.^{+37}_{-29}$	1217 ± 5	1	0.2	<21	12.1 ± 0.4
^{82}Ga	436	$610.^{+83}_{-72}$	599 ± 2	21	2.5	30 ± 8.0	22.3 ± 0.22

error budget are obtained for $^{75-77}$Ni and $^{77-79}$Cu with parent P_n values and daughter half-lives being the dominant sources.

IV. RESULTS FOR P_n VALUES

P_n values were determined from the number of β-n coincidences $N_{\beta n}$ detected within a correlation time τ after implantation using

$$P_n = \frac{N_{\beta n} - N_{\beta nb} - N_{\beta nd}}{\epsilon_\beta \epsilon_n \tilde{N}_\beta} \tag{1}$$

ϵ_β and ϵ_n are β and neutron detection efficiencies, respectively. The expected number of detected β-n background events $N_{\beta nb} = r_{\beta nb} N_{\rm imp} \tau_{\rm corr}$ can be calculated from the background rate $r_{\beta nb}$, the correlation time $\tau_{\rm corr}$, and the number of implanted ions $N_{\rm imp}$. The number of actual parent β decays $\tilde{N}_\beta = N_{\rm imp}(1 - \exp^{-\lambda \tau_{\rm corr}})$ can be determined from the known parent β-decay rate λ. $N_{\beta nd}$ are neutrons from β-delayed neutron emission of daughter nuclei, which can be significant in some of the cases studied here. It can be determined from

$$N_{\beta nd} = N_{\rm imp} \epsilon_n \epsilon_\beta [(1 - P_n) n_0 + P_n n_1], \tag{2}$$

with n_0 and n_1 given by

$$n_x = \frac{P_{nx} \lambda \lambda_x}{\lambda_x - \lambda} \left(\frac{1 - \exp^{-\lambda \tau_{\rm corr}}}{\lambda} - \frac{1 - \exp^{-\lambda_x \tau_{\rm corr}}}{\lambda_x} \right). \tag{3}$$

Indices $x = 0, 1$ indicate the daughters reached without and with neutron emission of the parent, respectively. λ is the parent decay rate, and λ_x and P_{nx} are daughter decay rates and P_n values, respectively. Note that $N_{\beta nd}$ does depend on the unknown parent P_n value. Equation (1) therefore needs to be rearranged to calculate P_n (see also Ref. [28]).

The neutron detection efficiency ϵ_n has been measured for a number of neutron energies in a separate experiment at the University of Notre Dame using the ^{13}C(α,n), ^{11}B(α,n), and ^{51}V(p, n) reactions. In the case of ^{13}C(α,n) and ^{10}B(α,n), the neutron production was inferred from the well-known properties of narrow resonances and a measurement of the beam current using a Faraday cup with electron suppression, while in the case of ^{51}V(p, n) the neutron yield was determined by offline counting of the induced ^{51}Cr activity. In addition, the detection efficiency was also determined with a calibrated ^{252}Cf source. Calibration measurements using the same ^{252}Cf source were also performed before and after the experiment reported here. The details of the efficiency calibration are discussed in Ref. [50], see also Ref. [28]. The NERO efficiency as a function of neutron energy is constant for low energies and drops for increasing neutron energies beyond $\approx$1 MeV. The energy of each neutron detection event is recorded to monitor correct operation of the detector system and setting of the detection thresholds, but does not contain information about the initial neutron energy because of the thermalization process. Therefore, theoretical assumptions about the maximum neutron energy have to be made. From numerous past studies, it is well known that β-delayed neutron spectra for medium to heavy nuclei are compressed at energies below $\approx$800 keV, often below 500 keV (for example, in Ref. [53]; see also more detailed discussion and references in Ref. [28]). The reason is the phase space for β decay that strongly favors

neutron-emitting states just above the neutron threshold, and a tendency for neutron decay into excited states in the final nucleus. In addition, we used our shell model calculations [47] to estimate maximum neutron energies for $^{74-76}$Ni and $^{78-79}$Cu. These calculations predict neutron energies in the range of 0.9–1.2 MeV when assuming the neutron decay of the daughter states populated by β decay proceeds to the ground state. This assumption obviously leads to an overestimation of the neutron energies. We adopt a conservative upper limit of 1.2 MeV for the neutron energies in this experiment and adopt the corresponding efficiency range of 33% to 41% as systematic error, resulting in $\epsilon_n = 37\% \pm 4\%$.

The β-n neutron background rate $r_{\beta nb}$ was determined from the β-n coincidence events among the same β-type events that were used to determine the β background. It was found that across the detector, the ratio of β-n to all β-type events was constant. We therefore determined this ratio for each run, and applied it to the position-dependent β-background rate used for the half-life analysis to obtain a position- and run-number-dependent β-n background rate. The β-n to β event ratio was on average about 4% on the first day of the experiment with significant scatter on an hourly time scale, and increased then to about 7% This is about 70 times larger than expected from random coincidences with the NERO singles neutron background rate (which was the same with and without beam) of 5 s^{-1} and the 200 μs β-n correlation time window. A possible explanation is the light ion contamination in the radioactive beam that deposits energies similar to β particles in the DSSD and might emit neutrons when interacting with the detector stack. A majority of such events were discarded as they passed through the entire detector stack and were therefore readily vetoed, but the remainder might have created a correlated β-n background. Such an enhanced background was also observed in a previous NSCL experiment with a similar setup [26]. Background from random coincidences between actual correlated parent and daughter β decays and uncorrelated neutrons was also considered, but found to be negligible in all cases.

The resulting P_n values are listed together with the number of detected β-n coincidences and the expected background neutrons in Table I. In most cases the statistical error of the number of detected neutron events dominates the error entirely. For the cases with high statistics, the other major contribution to the error is the uncertainty in the neutron detection efficiency. It becomes comparable to the statistical error for ^{78}Cu and dominates the uncertainty for ^{77}Cu. Only in the case of ^{74}Co is there another significant (more than 10%) contribution to the error. Here the uncertainty of the P_n value of the daughter, ^{74}Ni, contributes as well. Uncertainties in background rate, β efficiency, number of implanted ions, and daughter decay rates turn out to be negligible in all cases.

V. DISCUSSION

Figures 3–7 show our new half-lives and P_n values together with previous measurements. We include the half-lives of the neutron-rich Ni isotopes that were published and discussed earlier [25]. We now present additional half-life data for

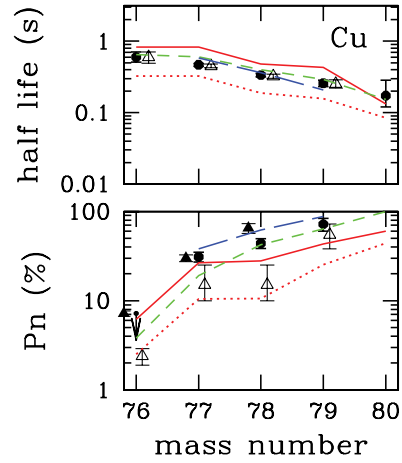

FIG. 3. (Color online) Half-lives and P_n values for the Cu isotopes measured in this work (solid black circles) compared with previous work (open black triangles), and theoretical predictions from QRPA97 [58] (solid red line), QRPA03 [42] (dotted red line), CQRPA [45] (short dashed green line), and OXBASH shell model (see text) (long dashed blue line). The experimental results from Ref. [57] are added as solid black triangles.

neutron-rich Co, Cu, Zn, and Ga isotopes, including the first measurement of the half-lives of ^{75}Co and ^{80}Cu. In most cases there is excellent agreement with previous measurements, except for the ^{79}Zn half-life, for which we obtain a significantly shorter value. It has been speculated in the past that the existence of an isomer in ^{79}Zn cannot be excluded [54]. As the population of isomers depends on the production mechanism, this could lead to differences in measured half-lives between our technique and previous measurements using the isotope separator on-line (ISOL) method for isotope production.

In addition to the half-lives, we also obtained P_n values or upper limits for most of the isotopes in the beam. For $^{73-75}$Co and $^{74-77}$Ni, these are the first direct measurements of β-delayed neutron emission. In the case of $^{77-79}$Cu, our measurements are more precise and systematically larger than previous work [55]. As stated by the authors, those experiments at CERN ISOLDE were difficult due to the

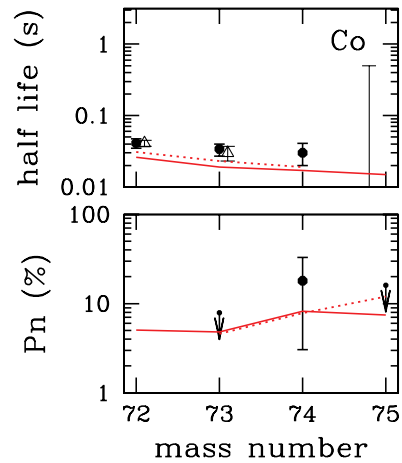

FIG. 4. (Color online) Same as Fig. 3, but for the Co isotopes.

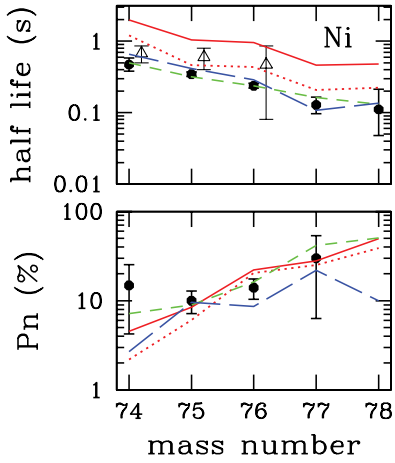

FIG. 5. (Color online) Same as Fig. 3, but for the Ni isotopes.

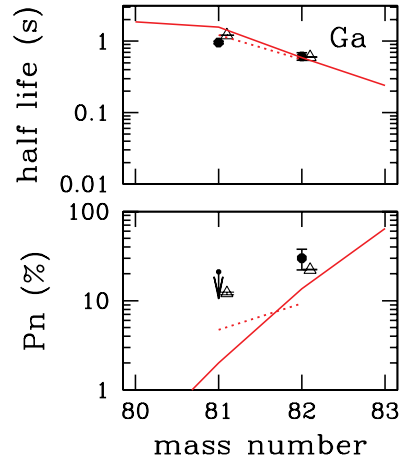

FIG. 7. (Color online) Same as Fig. 3, but for the Ga isotopes.

chemical nonselectivity of the plasma ion source, and have large uncertainties. Our P_n value for ^{79}Zn and ^{81}Ga as well as the upper limits for ^{80}Zn and ^{81}Ga are compatible with previous work. In the case of ^{81}Zn, our P_n value is larger than the literature value [55]. This is in line with new data from ISOLDE indicating a P_n value of larger than 10% for ^{81}Zn [56].

Recently, Mazzocchi *et al.* [52] reported preliminary lower limits for the P_n values of ^{73,74}Co of $9 \pm 4\%$ and $26 \pm 9\%$, respectively, from a γ-ray spectroscopy experiment. Within their uncertainties, these limits are compatible with our data, albeit only barely in the case of ^{73}Co, which would have to have P_n between 5% and 8% to be compatible with both our upper limit and their lower limit.

After completion of this work, new experimental P_n values for $^{76-78}$Cu obtained by β-delayed γ-ray spectroscopy have been reported [57] (see Fig. 3). The reported value for ^{76}Cu of $7.0 \pm 0.6\%$ is consistent with our upper limit. For ^{77}Cu, a rather precise value of $30.0 \pm 2.7\%$ was obtained, in excellent agreement with our result. For ^{78}Cu, the reported result of $65 \pm 8\%$ is significantly larger than our measurement. This might reflect the difficulty of obtaining a reliable P_n value via

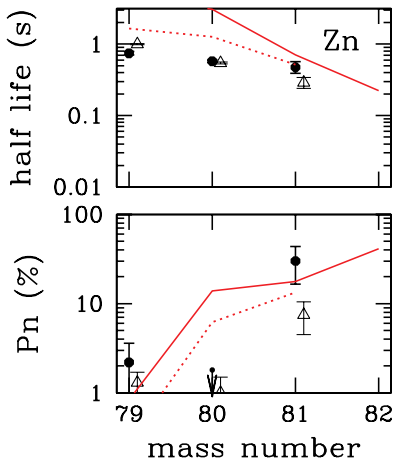

FIG. 6. (Color online) Same as Fig. 3, but for the Zn isotopes.

γ-ray spectroscopy in this particular case, as indicated by the authors [57].

In Figs. 3–7, our experimental results are compared with various theoretical calculations. The shell model calculations have been performed using the JJ4B effective interaction [59] for the $p_{3/2}f_{5/2}p_{1/2}g_{9/2}$ model space on top of a ^{56}Ni inert core. JJ4B has been developed starting from a realistic *G*-matrix interaction based on the Bonn-C *NN* potential together with core-polarization corrections [46]. It has been fitted to reproduce new experimental data separately for $^{57-78}$Ni isotopes (purely neutron interaction) and for $N = 50$ (^{79}Cu–^{100}Sn) isotones (purely proton interaction). This interaction has been extended further to incorporate the proton-neutron degree of freedom. The new version of the effective interaction JJ4B [59] takes into account information about 450 states in 73 nuclei including recent experimental data for Cu, Zn, Ga, Ge, As, Se, Br, and Kr in the vicinity of ^{78}Ni.

The number of chosen orbitals in these calculations is sufficient to achieve a satisfactory description of binding energies, neutron separation energies, and known excitation spectra for neutron-rich nuclei in the considered region. However, we find that to reproduce the half-lives and P_n values of neutron-rich Ni, Zn, and Cu isotopes, the Gamow-Teller (GT) operator has to be renormalized by a factor of 0.37, instead of the expected factor of 0.75 for this mass region. Such a strong renormalization of the GT operator indicates that shell model configurations responsible for considerable amounts of GT strength are not accounted for. Such configurations can be attributed to the excluded $f_{7/2}$ orbital, which is connected to its spin-orbit partner, $f_{5/2}$, by a very strong GT matrix element. Indeed, a test calculation in an enlarged model space that includes the proton $f_{7/2}$ orbital and uses a ^{48}Ca core has been performed with a combined effective interaction [60] and confirms that the exclusion of the $f_{7/2}$ orbital in the model space represents a strong limitation. This demonstrates the importance of β-decay data, including P_n values, in testing shell model calculations far from stability.

A global nuclear structure model is needed for astrophysical applications that is not limited to nuclei within a specific model space or near shell closures. We therefore compare our data to theoretical results from the global, universal

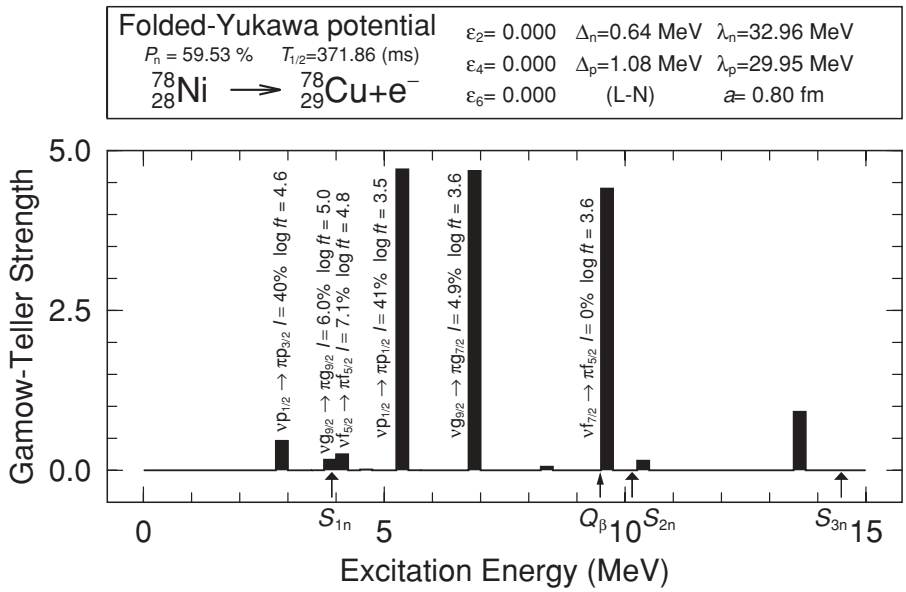

FIG. 8. (Color online) Calculated GT β-strength for ^{78}Ni. We indicate by wide arrows the $1n$, $2n$, and $3n$ neutron separation energies in the daughter ^{78}Cu following the decay of ^{78}Ni. Only states below Q_β are accessed in the decay. The figure is further discussed in the text.

quasiparticle random-phase approximation (QRPA) model, the details of which can be found in Refs. [42,58,61,62]. This model considers GT β-decay transitions from a parent nucleus to the accessible states in the daughter. The starting point is to calculate nuclear wave functions for the ground-state shape of the nucleus in a folded-Yukawa single-particle model. Ground-state shapes are taken from the finite range droplet model (FRDM) [63]. The decay rates are obtained as matrix elements of the GT operator between parent and daughter states in a QRPA with pairing and GT residual interactions. A global table of calculated β-decay half-lives and β-decay-delayed neutron emission rates was published in 1997 [58]. For that calculation, β-decay Q values had been obtained from the 1989 Atomic Mass Evaluation [64] when available, otherwise from the FRDM [63]. In our comparisons with experimental data, we denote this theoretical data set QRPA97.

Subsequently several enhancements have been made to this model, resulting in a new dataset QRPA03 [42]: An empirical spreading was applied to the Gamow-Teller strength function, and for nuclei near-magic numbers, an exact spherical shape was assumed instead of the weakly deformed shapes obtained for these nuclei in the FRDM [63]. In addition, a first-forbidden strength distribution as predicted by the gross theory [65,66] was added. Compared to the allowed Gamow-Teller strength, which over a given energy range is represented by relatively few strong peaks, the first-forbidden strength with its numerous small densely spaced peaks to a good approximation constitutes a "smooth background." It is therefore a reasonable approach to calculate the GT transitions in a microscopic QRPA approach and the first-forbidden (ff) transitions in a macroscopic statistical model, in analogy with the macroscopic-microscopic method used for mass models. The experimental masses used to determine the Q_β value were from Ref. [67] when available.

We can now compare both QRPA97 and QRPA03 with our new experimental data in the Co–Zn region. Overall, QRPA03 agrees better with our set of measurements, with the exception of the Cu isotopes, where, compared to QRPA97, the discrepancies increased, especially for the β-delayed neutron-emission probabilities (Fig. 3).

There are several possibilities for the origin of the discrepancies. The calculated half-life depends critically on the Q_β. For example, for ^{78}Ni, a change of Q_β of 1 MeV would change the half-life by roughly a factor of 2. As the half-life depends on a few low-lying transitions, a 1 MeV change in the main low-lying β strength just below 3 MeV (see Fig. 8) would have a similar effect. P_n values can be even more sensitive to the exact location of transitions in the strength distribution, in particular in a case like ^{78}Ni, where there is significant strength right around the one-neutron separation energy. Therefore, calculated P_n values are extremely sensitive to small variations in the calculated strength distribution near S_{1n}, and no model can predict accurately the energy levels or strength at these relatively high energies.

In addition, the strength distribution depends on deformation and on whether one includes first-forbidden transitions. This is illustrated in Table II. Clearly, when the GT-only transitions are fast (the first three rows), then adding ff transitions has a small effect. Fast GT transitions correspond to low-lying GT strength. Therefore adding a small ff component at these energies has little effect. In the case of long half-lives (last four rows), the effect of including ff transitions is more substantial. One could perhaps argue that a standard single-particle level diagram for this region of nuclei reveals no obvious candidates for such first-forbidden decays. Figure 8 indicates the main single-particle component of the strongest transitions. However, we should recall that the residual pairing and Gamow-Teller interactions considerably change both the energy and wave-function structure from the simple single-particle picture. Therefore a single-particle level diagram can only provide rough guidance to β-decay properties. More realistic nuclear interactions might well yield a level structure that contains first-forbidden decays to low-lying states. We also note that the effect of even fairly weak deformation can be significant.

TABLE II. Calculated β-decay half-lives and delayed-neutron-emission probabilities for four assumptions: (1) GT transitions and calculated ground-state shape, (2) GT transitions and spherical ground-state shape, (3) GT + ff transitions and calculated ground-state shape, and (4) GT + ff transitions and spherical ground-state shape.

Z	A	ϵ_2	$T_{1/2}$ (ms)				P_n (%)			
			GT		GT + ff		GT		GT + ff	
			Def.	Sph.	Def.	Sph.	Def.	Sph.	Def.	Sph.
27	73	0.092	27	33	25	30	5.34	2.82	6.94	4.59
27	74	0.117	18	26	16	22	9.30	4.75	10.19	7.76
27	75	0.092	15	20	13	18	7.17	5.68	10.41	11.98
28	75	0.058	1053	818	539	460	9.93	13.27	5.86	6.06
28	76	0.050	1064	674	585	433	25.94	36.18	16.97	20.49
28	77	0.050	428	370	226	207	33.58	35.16	22.80	25.17
28	78	0.025	371	371	228	224	38.26	59.53	28.69	39.06
29	76	0.117	734	463	435	318	8.06	1.28	4.74	2.46
29	77	0.083	827	417	505	318	32.81	10.40	19.30	10.38
29	78	0.075	386	289	224	187	34.82	11.16	19.79	10.60
29	79	0.050	391	224	223	155	46.32	18.97	38.07	25.24
29	80	0.075	103	160	64	84	58.46	100.00	51.53	56.62
30	79	0.067	4991	3591	1869	1647	1.29	1.76	0.29	0.34
30	80	0.042	3796	2505	1580	1259	20.91	4.04	5.72	6.19
30	81	0.075	707	3160	325	517	19.53	43.42	11.34	13.38
31	82	0.083	539	2062	304	553	14.43	34.76	9.03	9.32

It is therefore noteworthy that the global model still reproduces measured P_n values to within a factor of 3. The good global agreement between calculated and measured P_n and $T_{1/2}$ values is obtained, although *no model parameter* was varied to adjust the model to these experimental quantities.

Nevertheless the global QRPA calculations do show a significant underprediction of the high P_n values for the Cu isotopes found in this experiment and in Ref. [57], pointing to some issue in this model for this particular region. As discussed above, there are a number of possible reasons that could lead to such a deviation. One such possibility is uncertainty in the nuclear masses. Since QRPA03, the masses of the Zn daughter isotopes out to ^{81}Zn have been determined with high-precision Penning trap measurements [68,69]. As we do not mix theoretical and experimental masses to determine Q values, this does not affect the β-decay Q values, but it allows a precise determination of the neutron separation energies of the Zn isotopes, which are needed to determine the Cu P_n values. A recalculation with these new masses leads only to 10–30% changes compared to QRPA03, by far too small to explain the observed discrepancy. Furthermore, in the case of ^{76}Cu, both the β-decay Q values and daughter neutron separation energies are known experimentally with keV precision in the QRPA03 calculation. Clearly, the underprediction of P_n (with the new value of $7.3 \pm 0.6\%$ [57]) and half-life is already present in ^{76}Cu. Therefore, masses are unlikely to be the explanation for this problem. The extensive γ-ray data from Ref. [57] for ^{77}Cu, once published, might help test the calculated strength functions in more detail to determine the cause of this problem.

Our recalculation of the QRPA predictions with updated Zn masses had a significant impact on the predicted Zn half-lives, where the β-decay Q values are now known experimentally. For example, for ^{79}Zn, the β-decay Q value increases from 8.68 MeV as predicted by the FRDM to 9.08 ± 0.1 MeV, decreasing the predicted half-life from 1.6 to 1.0 s. Similarly, the ^{80,81}Zn half-lives decrease from 1.3 and 0.52 to 1.0 and 0.35 s, respectively. Overall, this reduces the discrepancy between experiment and theoretical prediction significantly.

Finally, we compare our new data with the continuum QRPA (CQRPA) calculations from Borzov [45]. His treatment is limited to spherical nuclei and is not global, but does include a *pn* interaction in the particle-particle channel and a microscopic calculation of the first-forbidden strength. Table II shows that the assumption of spherical shapes may be inappropriate, since even the modest deformations predicted for his region are expected to have a substantial effect on half-lives and P_n values. The predictions of half-lives and P_n values by Borzov show overall very good agreement with our experimental results. Borzov finds that in his model first-forbidden transitions play only a minor role around ^{78}Ni as long as $N \leqslant 50$. However, the CQRPA model does significantly underpredict the P_n values of ^{76}Cu and ^{77}Cu, while there is excellent agreement for ^{78}Cu and ^{79}Cu.

Motivated by their new experimental P_n values for $^{77-78}$Cu, Winger *et al.* [57] argue that this underprediction is an indication of the inversion of the $\pi 2p_{3/2}$ and $\pi 1f_{5/2}$ single-particle orbitals. CQRPA model calculations where these orbitals are inverted indeed lead to larger P_n values, though no half-life data are presented that would allow us to verify consistency with experimental half-lives. However, our P_n value for ^{78}Cu is significantly lower than the experimental value reported in Ref. [57]. While the old CQRPA results are in agreement with our measurement, the new CQRPA value of 53% is somewhat high. In addition, the old CQRPA results are also in excellent agreement with our new P_n value for ^{79}Cu. Nevertheless, there is other experimental evidence for such a

level inversion to occur for Cu isotopes at ^{75}Cu and beyond [70] thereby justifying the modifications of the CQRPA model.

VI. *r*-PROCESS CALCULATIONS

With our new data and recent precision mass measurements around ^{80}Zn [68,69], the nuclear physics needed to model the *r*-process around $A = 80$ is now to a large extent experimentally determined. We can therefore test *r*-process models in this particular mass region against observations with greatly reduced nuclear physics uncertainties.

It is quite challenging to understand the origin of the elements in this mass region, as not only all major neutron-capture processes, the weak and strong *s*-process and the *r*-process, can contribute, but charged-particle reaction sequences can reach this mass region as well. Indeed, one class of *r*-process models, the neutrino-driven wind scenario in core collapse supernovae, predict that nuclei in this region are produced by a combination of charged-particle and neutron-induced reactions. Nevertheless, we can ask whether *r*-process models characterized by a neutron capture and β-decay reaction sequence in the $A = 80$ mass region are now able to reproduce the observed solar *r*-process abundances in this region.

To address this question we use a classical *r*-process model that simulates a series of neutron exposures of Fe seed nuclei with neutron density n_n, temperature T, duration τ, and weight ω. It has been shown that such a model can reproduce the observed solar abundance pattern reasonably well employing power-law relationships $\omega(n_n) = a_1 n_n^{a_2}$ and $\tau(n_n) = a_3 n_n^{a_4}$ leaving only three free parameters plus an overall normalization [71]. The temperature $T = 1.35$ GK is kept constant and is the same for all components representing a typical *r*-process freeze-out temperature. The model we use adopts the waiting point approximation and assumes a sudden freeze-out with decay back to stability once all exposures have been applied. The fact that the site of the *r*-process is still unknown and that a wide range of scenarios have been proposed motivates the use of this simple site-independent model. The classical model can simulate well the final local neutron-capture flow in an *r*-process scenario at freeze-out, which tends to dominate the features of the final abundance pattern. Of course, further modifications of the abundance pattern can occur during freeze-out, but this effect is highly model dependent. It therefore makes sense to explore the agreement of a simple *r*-process model with observations. Once the nuclear physics is fixed, major disagreements with observations might indicate an entirely different *r*-process mechanism for the mass region in question, while smaller deviations might reveal additional, site-specific effects, such as an extended freeze-out.

Figure 9 shows results from an *r*-process calculation, where the four model parameters have been fitted to reproduce the solar *r*-process residuals from Arlandini *et al.* [72]. These *r*-process residuals have been obtained by subtracting from the observed solar abundances a main *s*-process component calculated with a classical *s*-process model and a weak *s*-process component. In the $A = 80$ mass region, this solar *r*-process abundance distribution is very similar to the one obtained with a set of realistic stellar *s*-process models and updated solar abundances [73]. Our baseline model calculation with model parameters $a_1 = 4224.74$, $a_2 = -0.082$, $a_3 = 788.86$, and $a_4 = 0.0089$ uses the nuclear masses from the 2003 Atomic Mass Evaluation [74], including their extrapolations, updated with the new masses in the Zn region [68,69]. Masses of more exotic nuclei are taken from the ETFSI-Q mass model, which has been shown to be well suited for *r*-process calculations. We also performed calculations using the FRDM mass model that lead to very similar results in the $A = 80$ mass region and to the same conclusions. Experimental β-decay data, including P_n values, are taken from the National Nuclear Data Center (NNDC) [75] when available, otherwise our theoretical QRPA03 data are used. For comparison, we then run the same calculation with our updated β-decay properties from this study. We also show a

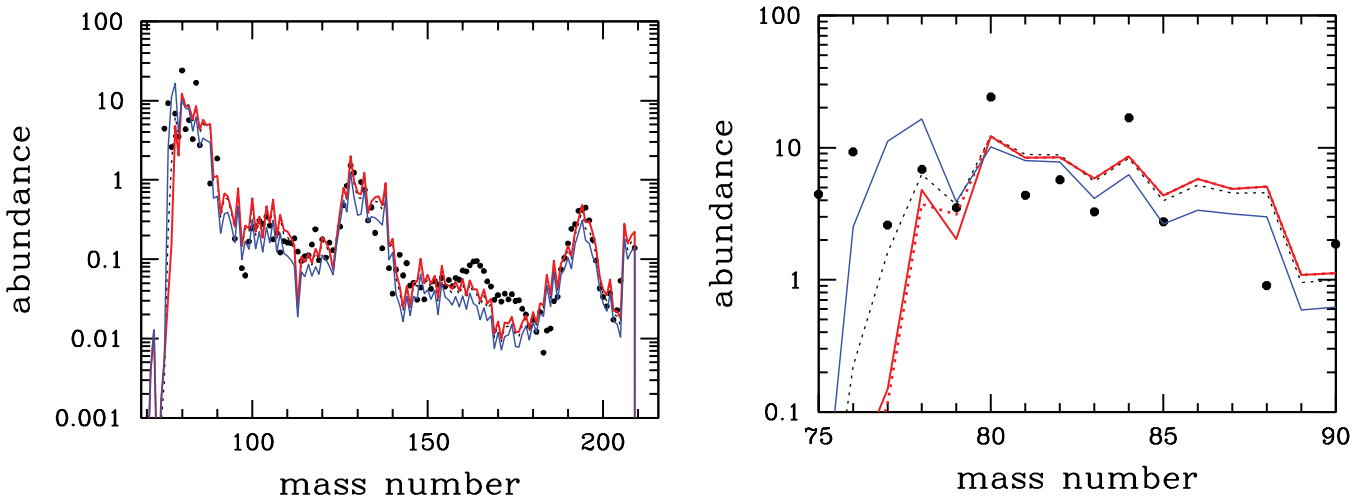

FIG. 9. (Color online) Abundances calculated with a classical *r*-process model using previously known decay data (dotted black line) and the new data from this work (thick solid red line). The thin solid blue line indicates a calculation with the large ^{78}Ni half-life predicted by QRPA97. The thick dotted red line shows results using the new half-lives from our work, but the old P_n values. Solar *r*-process abundances are shown as black data points.

calculation using the large ^{78}Ni half-life predicted in our earlier QRPA97 model.

The global effects of implementing our new experimental data are rather modest. However, the half-life of ^{78}Ni clearly plays an important role, and the large ^{78}Ni half-life of QRPA97 leads to noticeable changes across all masses, including the $A = 195$ peak region. Our measurement of the half-life of ^{78}Ni now excludes such a long half-life with certainty.

In the $A = 80$ region, changes are more significant. Our new data lead to a more pronounced odd-even effect for $A = 78, 79, 80$ that agrees better with observations. As Fig. 9 shows, our shorter ^{78}Ni half-life actually leads to a weaker odd-even effect between $A = 78$ and 79, but the larger P_n values for the Cu isotopes, especially ^{79}Cu, more than compensate and are therefore important to obtain a better fit. The need for large P_n values, especially for ^{79}Cu, in order to reproduce the pronounced odd-even effect in the r-process abundances has already been pointed out in earlier studies based on theoretical predictions of half-lives and P_n values [76].

Overall, with the masses and decay data for $A \leqslant 81$ now available, the $A = 80$ region can be reproduced quite well. The agreement is very good for $A = 78, 79, 80$ where some experimental data are now available. On the other hand, some problems become apparent in the $A = 81$–90 mass range. Because of the lack of experimental constraints on the nuclear physics in this region, a nuclear physics explanation cannot be excluded yet. In this region, most of the relevant masses and most of the relevant β-decay half-lives beyond $A = 84$ are unknown. Clearly more experimental work needs to be done to extend the mass region of reliable nuclear physics over the entire $A = 80$ abundance peak area.

Even in the $A = 78$–80 area, there are still some remaining nuclear physics uncertainties. The most important nuclear physics data at the $N = 50$ shell closure are the half-lives of the major $N = 50$ waiting points, ^{78}Ni, ^{79}Cu, and ^{80}Zn and the nuclear masses for the isotopic chains, where the neutron-capture flow might begin to cross the $N = 50$ shell closure. Owing to the rather large drop in neutron separation energy across the $N = 50$ shell gap, it is clear that regardless of the mass model adopted, for the Ni and Cu isotopes, the neutron densities required for the reaction flow to cross $N = 50$ ($n_n > 10^{24,26}$ for the Cu, Ni isotopic chains, respectively) are much higher than the neutron densities that produce the bulk of the $A = 80$ isotopes. Therefore, for the calculation of abundances around $A = 80$, precision masses to characterize the breakout beyond $N = 50$ in detail are mainly needed for Zn and Ga. For these isotopic chains, masses are needed across $N = 50$ out to $N = 52$ because of the odd-even effect of the neutron separation energies. In addition, P_n values are needed for all $A = 78$–80 waiting points and their decay daughters. With our data and previous work, all of these quantities are now experimentally known, except for the mass of ^{82}Zn, which might introduce some uncertainty concerning the ^{80}Zn waiting point. This has been discussed in detail in Ref. [68]. In addition, the measured ^{78}Ni half-life still has a large error bar. While the rather long half-life predicted by QRPA97 is now excluded, the half-life change that leads to the changed $A = 78$ abundance indicated in Fig. 9 is actually of the order of the experimental uncertainty. Therefore, a more precise ^{78}Ni half-life would be desirable. The P_n value of ^{78}Ni might have some influence on the result as well and should be determined experimentally.

Finally, we also explore the role of nuclear physics in the ^{78}Ni region in a more site-specific r-process model, the so-called high-entropy wind (HEW) scenario [4–6,77–81]. The model is inspired by the conditions expected near the proton-neutron star forming in a core collapse supernova shortly after the explosion. The high neutrino luminosity is thought to drive outflows of strongly heated, low-density matter (hence high entropy) that at late times become neutron rich. While this is one of the most promising candidates for an r-process scenario, realistic models based on conditions obtained in current supernova models do not lead to a full r-process. We therefore use the simplified parametrized model of Refs. [78,81] that follows a set of one-dimensional adiabatic expansions (components), each characterized by an entropy per baryon S, an initial electron abundance Y_e, and an expansion velocity v. Nuclear reactions are followed with a full reaction network including β-decay properties and all neutron, proton, and γ-induced reactions, but neglecting neutrino interactions and fission. One possible choice of parameters that leads to a successful r-process is to keep the same realistic values of $Y_e = 0.45$ and $v = 7500$ km/s for all components, but choose an equidistant set of entropies that ranges up to about $S/k \sim 250$, larger than predicted by supernova models. When assuming that equal amounts of material are processed by each component, such a model has been shown to reasonably reproduce the solar r-process residuals [78,81]. We use the same β-decay rates and P_n values employed in our classical model calculations. Neutron- and charged-particle-induced reaction rates are taken from NON-SMOKER statistical model predictions [82] using the FRDM mass model. γ-induced reactions are calculated from their inverse capture reactions via detailed balance.

In HEW models, r-process seed nuclei are produced by combined charged-particle and neutron-induced processes in the $A \sim 90$ region close to stability. As this is already beyond the ^{78}Ni region, one might expect that β-decay properties near ^{78}Ni do not play a role. Our calculations show, however, that at high entropies around $S/k = 200$, where neutron to seed ratios become high enough to produce the heavier r-process elements, ^{78}Ni becomes part of the r-process path. Figure 10 shows the abundance distribution for $S/k = 200$ with the previous nuclear database, and with our new experimental results. It turns out that the change is entirely due to our new, shorter ^{78}Ni half-life (110 ms instead of 224 ms). For comparison, we also show a calculation with the older, longer ^{78}Ni half-life (477 ms) predicted in Ref. [58]. Clearly a long ^{78}Ni half-life reduces the $A = 78$ production, but increases the production of $A = 100$–120 nuclei at $S/k \sim 200$. Interestingly, the production of very heavy r-process nuclei is slightly suppressed by a shorter ^{78}Ni half-life, contrary to what one would expect naively and opposite from the behavior in the classical model. Nevertheless, the impact of the ^{78}Ni half-life on the final abundances, once all entropy components have been added up, is rather small. Figure 11 shows the ratio of our new abundances to what one obtains with the long ^{78}Ni half-life from Ref. [58]. Besides the significant change at $A = 78$, there

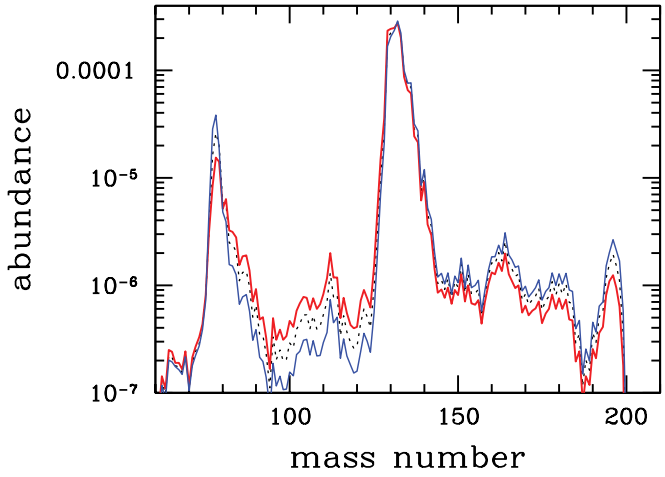

FIG. 10. (Color online) Abundances calculated with the HEW r-process model for a single entropy component with $S/k = 200$. Results based on the data from this work (^{78}Ni half-life of 110 ms) (thick solid red line) are compared with results based on previously available data (^{78}Ni half-life of 224 ms) (thin solid blue line) and previously available data with the long ^{78}Ni half-life of 477 ms from Ref. [58] (black dotted line).

is a 10% increase at $A = 130$ (where $S/k = 200$ makes its largest contribution) and a 10% suppression of very heavy nuclei. This modest sensitivity of the final abundances reflects the rather narrow entropy range between $S/k \sim 190$ and 210 that is broadly influenced by ^{78}Ni. Effects for higher entropies are still significant but only below $A \sim 130$ where those high-entropy components do not contribute much. However, it is likely that critical waiting points such as ^{78}Ni in the case of $S/k \sim 200$ do exist also for the other entropy components. It will be important to identify and measure these waiting points to obtain more reliable HEW r-process calculations. In addition to the already known $N = 50$ isotopes ^{80}Zn and ^{79}Cu, our first measurement of the ^{78}Ni half-life is an important further step toward this goal.

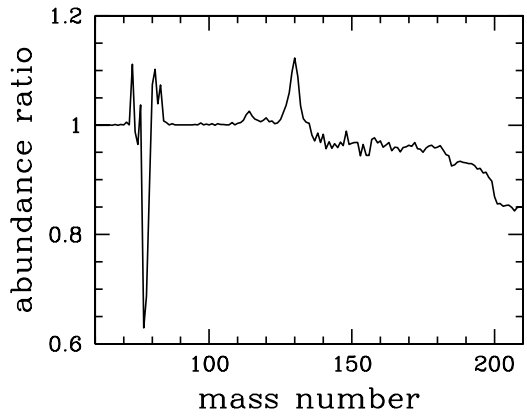

FIG. 11. (Color online) Ratio of final HEW abundance distributions summed over all entropy components calculated with our new data including a shorter ^{78}Ni half-life of 110 ms to what one obtains using previously available data and the long ^{78}Ni half-life of 477 ms from Ref. [58].

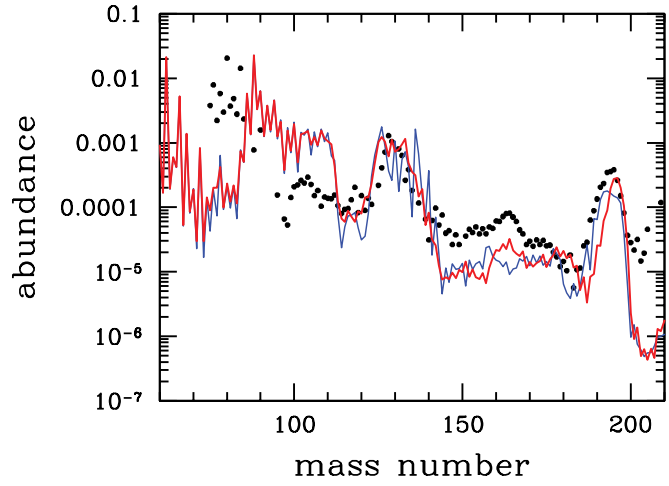

FIG. 12. (Color online) HEW abundance distributions summed over all entropy components using our new data (thick solid red line) and setting all P_n values to zero (thin solid blue line) compared with the solar r-process residuals (black filled circles).

Using our new P_n values instead of the old ones does not lead to significant changes in the calculated abundances for our choice of HEW model parameters. In principle, one can expect a reduced impact of β-delayed neutron emission compared to the classical model, as neutrons are present at later times potentially reversing the effects via neutron capture. Once the neutrons are exhausted, the r-process path tends to be already closer to stability where P_n values are smaller. To explore the impact of P_n values in HEW calculations, we run a simulation without any β-delayed neutron emission for comparison. This is similar to what has been done in Ref. [16] for the classical r-process model. The result is shown in Fig. 12 and demonstrates the importance of β-delayed neutron emission in HEW models. For $A < 110$ the impact is less pronounced, though for some mass chains significant changes of up to a factor of 2 do occur. On the other hand, P_n values play a critical role in shaping the $A = 130$ and $A = 195$ abundance peaks as well as the rare-earth-metal peaks.

Overall the impact of our new data on the synthesis of $A \sim 80$ r-process nuclei in our HEW model is rather modest, in contrast to what we found in the classical model. However, as has been discussed extensively in Ref. [78], and as can be seen in Fig. 12, our particular choice of HEW model parameters, especially our initial Y_e, clearly does not reproduce the solar r-process residuals below $A \sim 110$. Once this problem has been solved, the question of the relevance of the nuclear physics in the $A = 80$ region in HEW models should be revisited.

VII. SUMMARY

We have provided the first experimental P_n values for extremely neutron-rich Ni isotopes out to ^{77}Ni and a first half-life for ^{80}Cu. Our experimental P_n values for ^{77}Cu and ^{78}Cu confirm the finding of an experiment carried out in parallel to this study [57] that the previously reported P_n values are too small, though in the case of ^{78}Cu we find the discrepancy is somewhat smaller as reported in Ref. [57]. This

discrepancy is not too surprising given the large error bars and the difficulties encountered in these earlier measurements.

Given these discrepancies with earlier work, our measurement of the P_n value of ^{79}Cu is of particular importance because of the key role this nucleus plays in r-process models. We find that in this case, our new measurement agrees well with work reported earlier, indicating that the problems with earlier experiments are not necessarily of a general nature.

Our experimental data provide constraints for theoretical models used to understand the nuclear structure of the ^{78}Ni region. We find that recent shell model calculations as well as local continuum QRPA calculations describe the experimental data well. This gives us some confidence that such models can be used to investigate nuclear structure effects around ^{78}Ni. However, in the case of the shell model calculations, the required large GT quenching factor indicates the need for larger model spaces.

Our results also show that the global QRPA03 model used to predict nuclear structure input for astrophysical r-process calculations agrees with data within the expected theoretical uncertainty. The model exhibits some local deficiencies in the ^{78}Ni mass region, in particular for the P_n values of the neutron-rich Cu isotopes. More experimental data are needed to identify the nature of this problem. With our measurements, experimental decay data are now available for r-process calculations along the entire reaction path at $N = 50$. This includes our improved data on the branchings for β-delayed neutron emission of ^{78}Cu and ^{79}Cu, which are needed in r-process model calculations to reliably calculate the final abundances in the $A = 78$–79 mass range. Together with recent mass measurements around ^{80}Zn this now puts a three-isotope section of the r-process around $A = 80$ on a fairly solid experimental basis. Our r-process model calculations demonstrate that this narrow mass region of $A = 78$–80 turns out to be well reproduced with a neutron-capture flow based r-process. More experimental nuclear physics data beyond $A = 80$ are needed to broaden the mass range in which r-process models can be tested reliably, but for now neutron capture under typical r-process conditions cannot be excluded as a mechanism for the origin of the elements around $A = 80$ that are not made by the s-process.

We also show that the ^{78}Ni half-life does play a role in HEW r-process models. On the other hand, compared to the classical model, the HEW model seems to be less sensitive to P_n values in the Ni–Cu region, at least for our choice of parameters. We demonstrated that the P_n values of heavier nuclei do play a critical role in our HEW r-process model.

ACKNOWLEDGMENTS

This work was supported by NSF Grants PHY 08-22648 (Joint Institute for Nuclear Astrophysics), PHY 06-06007 (NSCL), and PHY 02-16783, by the Deutsche Forschungsgemeinschaft (DFG) under Contract KR 806/13, and by the Helmholtz Gemeinschaft under Grant VH-VI-061 (VISTARS).

[1] E. M. Burbidge *et al.*, Rev. Mod. Phys. **29**, 547 (1957).
[2] J. J. Cowan, F.-K. Thielemann, and J. W. Truran, Phys. Rep. **208**, 267 (1991).
[3] M. Arnould, S. Goriely, and K. Takahashi, Phys. Rep. **450**, 97 (2007).
[4] S. E. Woosley and R. D. Hoffman, Astrophys. J. **395**, 202 (1992).
[5] K. Takahashi, J. Witti, and H.-Th. Janka, Astron. Astrophys. **286**, 857 (1994).
[6] A. Burrows *et al.*, New Astron. Rev. **50**, 487 (2006).
[7] A. G. W. Cameron, Astrophys. J. **562**, 456 (2001).
[8] C. L. Fryer *et al.*, Astrophys. J. **646**, L131 (2006).
[9] K. Sumiyoshi *et al.*, Astrophys. J. **562**, 880 (2001).
[10] S. Wanajo *et al.*, Astrophys. J. **593**, 968 (2003).
[11] S. Rosswog *et al.*, Astron. Astrophys. **341**, 499 (1999).
[12] J. Pruet, S. E. Woosley, and R. D. Hoffman, Astrophys. J. **586**, 1254 (2003).
[13] R. Surman and G. C. McLaughlin, Astrophys. J. **618**, 397 (2005).
[14] P. Jaikumar, B. S. Meyer, K. Otsuki, and R. Ouyed, Astron. Astrophys. **471**, 227 (2007)
[15] C. Sneden, J. J. Cowan, and R. Gallino, Annu. Rev. Astron. Astrophys. **46**, 241 (2008).
[16] K.-L. Kratz *et al.*, Astrophys. J. **403**, 216 (1993).
[17] B. Pfeiffer *et al.*, Nucl. Phys. A **693**, 282 (2001).
[18] K.-L. Kratz *et al.*, Astrophys. J. **662**, 39 (2007).
[19] K.-L. Kratz *et al.*, Hyperfine Interact. **129**, 185 (2000).
[20] J. Shergur *et al.*, Phys. Rev. C **65**, 034313 (2002).
[21] B. Pfeiffer *et al.*, Prog. Nucl. Energy **41**, 39 (2002).
[22] O. Sorlin *et al.*, Nucl. Phys. A **719**, C193 (2003).
[23] I. Dillmann *et al.*, Phys. Rev. Lett. **91**, 162503 (2003).
[24] K.-L. Kratz *et al.*, Eur. Phys. J. A **25**, 633 (2005).
[25] P. Hosmer *et al.*, Phys. Rev. Lett. **94**, 112501 (2005).
[26] F. Montes *et al.*, Phys. Rev. C **73**, 035801 (2006).
[27] O. Arndt, Acta Phys. Pol. B **40**, 437 (2009).
[28] J. Pereira *et al.*, Phys. Rev. C **79**, 035806 (2009).
[29] T. Terasawa *et al.*, Astrophys. J. **562**, 470 (2001).
[30] K.-L. Kratz, Nucl. Phys. A **417**, 447 (1984).
[31] R. Grzywacz *et al.*, Phys. Rev. Lett. **81**, 766 (1998).
[32] W. F. Mueller *et al.*, Phys. Rev. C **61**, 054308 (2000).
[33] S. Franchoo *et al.*, Phys. Rev. C **64**, 054308 (2001).
[34] M. Sawicka *et al.*, Phys. Rev. C **68**, 044304 (2003).
[35] M. Sawicka *et al.*, Eur. Phys. J. A **22**, 455 (2004).
[36] M. Sawicka *et al.*, Eur. Phys. J. A **20**, 109 (2004).
[37] C. Mazzocchi *et al.*, Phys. Lett. B **622**, 45 (2005).
[38] J. Van Roosbroeck *et al.*, Phys. Rev. C **71**, 054307 (2005).
[39] J. Engel, M. Bender, J. Dobaczewski, W. Nazarewicz, and R. Surman, Phys. Rev. C **60**, 014302 (1999).
[40] J. M. Daugas *et al.*, Phys. Lett. B **476**, 213 (2000).
[41] H. Grawe *et al.*, Nucl. Phys. A **704**, 211c (2002).
[42] P. Möller, B. Pfeiffer, and K.-L. Kratz, Phys. Rev. C **67**, 055802 (2003).
[43] K. Langanke and G. Martinez-Pinedo, Rev. Mod. Phys. **75**, 819 (2003).
[44] N. A. Smirnova, A. De Maesschalck, A. Van Dyck, and K. Heyde, Phys. Rev. C **69**, 044306 (2004).
[45] I. N. Borzov, Phys. Rev. C **71**, 065801 (2005).
[46] A. F. Lisetskiy, B. A. Brown, M. Horoi, and H. Grawe, Phys. Rev. C **70**, 044314 (2004).

[47] A. F. Lisetskiy, B. A. Brown, and M. Horoi, Eur. Phys. J. A **25**, 95 (2005).
[48] D. J. Morrissey *et al.*, Nucl. Instrum. Methods B **204**, 90 (2003).
[49] J. I. Prisciandaro, A. C. Morton, and P. F. Mantica, Nucl. Instrum. Methods A **505**, 140 (2003).
[50] J. Pereira *et al.*, Nucl. Instrum. Methods A **618**, 275 (2010).
[51] G. Audi *et al.*, Nucl. Phys. A **729**, 3 (2003).
[52] C. Mazzocchi *et al.*, Eur. Phys. J. A **25**, 93 (2005).
[53] K.-L. Kratz *et al.*, Z. Phys. A **306**, 239 (1982).
[54] B. Ekström *et al.*, Phys. Scr. **34**, 614 (1986).
[55] K.-L. Kratz *et al.*, Z. Phys. A **340**, 419 (1991).
[56] U. Köster *et al.*, AIP Conf. Proc. **798**, 315 (2005).
[57] J. Winger *et al.*, Phys. Rev. Lett. **102**, 142502 (2009).
[58] P. Möller, J. R. Nix, and K.-L. Kratz, At. Data Nucl. Data Tables **66**, 131 (1997).
[59] B. A. Brown and A. F. Lisetskiy (private communication).
[60] A. F. Lisetskiy, B. A. Brown, and H. Schatz, *Proceedings of Capture Gamma-Ray Spectroscopy and Related Topics: 12th International Symposium*. AIP Conference Proceedings, edited by A. Aprahamian and A. Woehr, Vol. 819, pp. 483-486 (2006).
[61] J. Krumlinde and P. Möller, Nucl. Phys. A **417**, 419 (1984).
[62] P. Möller and J. Randrup, Nucl. Phys. A **514**, 1 (1990).
[63] P. Möller, J. R. Nix, W. D. Myers, and W. J. Swiatecki, At. Data Nucl. Data Tables **59**, 185 (1995).
[64] G. Audi, Midstream Atomic Mass Evaluation, 1989, with four revisions (unpublished).
[65] K. Takahashi, Prog. Theor. Phys. **47**, 1500 (1972).
[66] K. Takahashi, M. Yamada, and T. Kondoh, At. Data Nucl. Data Tables **12**, 101 (1973).
[67] G. Audi and A. H. Wapstra, Nucl. Phys. A **595**, 409 (1995).
[68] S. Baruah *et al.*, Phys. Rev. Lett. **101**, 262501 (2008).
[69] J. Hakala *et al.*, Phys. Rev. Lett. **101**, 052502 (2008).
[70] K. Flanagan *et al.*, Phys. Rev. Lett. **103**, 142501 (2009).
[71] J. J. Cowan *et al.*, Astrophys. J. **521**, 194 (1999).
[72] C. Arlandini *et al.*, Astrophys. J. **525**, 886 (1999).
[73] C. Travaglio *et al.*, Astrophys. J. **601**, 864 (2004).
[74] A. H. Wapstra, G. Audi, and C. Thibault, Nucl. Phys. A **729**, 129 (2003).
[75] J. K. Tuli, *Nuclear Wallet Cards*, 7th ed. (BNL, Upton, NY, 2005).
[76] K.-L. Kratz *et al.*, Z. Phys. A **336**, 357 (1990).
[77] B. S. Meyer and J. S. Brown, Astrophys. J. Suppl. **112**, 199 (1997).
[78] C. Freiburghaus *et al.*, Astrophys. J. **516**, 381 (1999).
[79] S. Wanajo *et al.*, Astrophys. J. **554**, 578 (2001).
[80] T. A. Thompson, A. Burrows, and B. S. Meyer, Astrophys. J. **562**, 887 (2001).
[81] K. Farouqi *et al.*, Astrophys. J. Lett. **694**, L49 (2009).
[82] T. Rauscher and F.-K. Thielemann, At. Data Nucl. Data Tables **79**, 47 (2001).